Synergistic reinforcing and cross-linking effect of thiol-ene-modified cellulose nanofibrils on natural rubber

Ge Zhu, Alain Dufresne

Synergistic reinforcing and cross-linking effect of thiol-ene-modified cellulose nanofibrils on natural rubber

Ge Zhu, Alain Dufresne*

Univ. Grenoble Alpes, CNRS, Grenoble INP, LGP2, F-38000, Grenoble, France

* Corresponding author:

Alain Dufresne (E-mail: *alain.dufresne@pagora.grenoble-inp.fr*)

Abstract

To achieve synergistic reinforcing and cross-linking effect across interface between hydrophilic nanocellulose and hydrophobic rubber, active thiol groups were introduced at reducing end of CNF while retaining hydroxyl groups on the surface, thus forming a percolation network in nanocomposites. The nanocomposites were obtained by casting/evaporating a mixture of dispersed modified CNF and NR in latex form, in which covalent cross-links were formed between thiol groups and double bonds of NR via photochemically initiated thiol-ene reaction. Strong interfacial interaction between NR matrix and end-modified CNF was characterized by Fourier-transform infrared spectroscopy. The structural and mechanical properties of the nanocomposites were evaluated by scanning electron microscopy, dynamic mechanical analysis and tensile tests. Compared to neat NR, the nanocomposite reinforced with 10 wt% modified CNF showed significantly higher values of tensile strength (0.33 to 5.83 MPa), Young's modulus (0.48 to 45.25 MPa) and toughness (2.63 to 22.24 MJ m^{-3}).

Keywords

Cellulose nanofibril, End modification, Thiol-ene reaction, Interfacial interaction, Mechanical properties

1. Introduction

Polymer nanocomposites consisting of a nanoscale reinforcing filler and polymer matrix have attracted researchers' great interest in the last few decades (Fu et al., 2018; Cao, Zhang, Lu, Luo, & Zhang, 2017; Chen, Huang, Gong, Xu, & Mou, 2017). The nanofiller helps to achieve better properties at lower volume fractions due to their large specific surface area compared to micrometer size particles. By using nanofillers (such as silica, carbon nanotubes, clay and graphene) (Cao, Huang, & Chen, 2018; Cao, Fan, Huang, & Chen, 2019; Jardin, Zhang, Hu, Tam, & Mekonnen, 2020), stronger reinforcement effects have been achieved in natural rubber (NR) composites. Among the potential nanofillers, nanocellulose, consisting of nanosized cellulose-based particles, is an elongated nanomaterial with high aspect ratio and high crystallinity. It has been widely studied due to its excellent mechanical properties, biocompatibility, renewability, sustainability and abundance.

NR is one of the most important elastic materials in daily applications due to its excellent strength, resilience, flexibility and elasticity (Xu, Zheng, Wu, Wang, & Fu, 2019; Liu, Cao, Yuan, & Chen, 2018; Gan et al., 2018). However, unfilled NR exhibits poor mechanical properties in terms of stiffness, so the incorporation of a nanofiller into NR matrix is often required (Smyth, García, Rader, Foster, & Bras,

2017; Pasquini, de Morais Teixeira, da Silva Curvelo, Belgacem, & Dufresne, 2010; Wu, Lu, Zhang, & Zhou, 2015). Smyth et al. (2017) and Pasquini et al. (2010) studied the reinforcing effect of cellulose nanocrystals (CNCs) on natural rubber and found that the performance of the obtained nanocomposites mainly depended on the properties of CNC, since the higher the aspect ratio, the better the reinforcing effect. Meanwhile, it was found that the formation of a rigid percolation network over a certain filler content greatly enhanced the reinforcement of the NR matrix (Peng et al., 2019; Tao, Dufresne, & Lin, 2019)

However, the increase in the mechanical properties of the nanocomposites by adding nanocellulose was still not very obvious and far from expectation due to inadequate interfacial interaction between nanocellulose and NR matrix. The nanocellulose surface contains a large number of hydroxyl groups, so the interfacial compatibility between hydrophilic nanocellulose and hydrophobic rubber matrix is poor and leads to aggregation of nanocellulose in the NR matrix. This insufficient interfacial adhesion between both components does not effectively transfer the stress from the continuous phase to the filler under mechanical loading. In order to improve the compatibility and enhance the interfacial adhesion between nanocellulose and the NR matrix, Parambath Kanoth et al. (2015) introduced sulfhydryl groups (-SH) on the surface of CNC and achieved reinforcement and cross-linking between the NR matrix and modified CNC by thiol-ene reaction. Goetz et al. (2009a, 2009b)) used poly(methyl vinyl ether-co-maleic acid)-polyethylene glycol as a matrix and

nanocellulose as a cross-linking agent to prepare cross-linked nanocomposites via the esterification reaction. The nanocellulose is trapped in the cross-linking network which prevents its aggregation, and the nanocomposite shows excellent mechanical properties. Therefore, the dispersion of the nanofiller within the host polymer matrix and the interfacial interactions between the nanofiller and the matrix are key properties for improving the properties of the nanocomposite. However, these strategies consume surface hydroxyl groups which are the basis of the exceptional reinforcing effect of these nanoparticles via the establishment of a nanofiller percolating network.

Here, we chose high aspect ratio cellulose nanofibrils (CNFs) as reinforcing nanofiller but also as cross-linking agent after end modification. In order to achieve the synergistic effect of strengthening and cross-linking across the interface, active thiol groups (-SH) were introduced at the reducing end of CNF, while retaining the hydroxyl (-OH) groups on the surface, giving CNFs the possibility to interact with each other and thus forming a stable percolating network in the nanocomposites. The nanocomposites were obtained by casting/evaporating a mixture of dispersed modified CNF and NR in latex form, in which covalent cross-links were formed between the thiol groups and double bonds of the NR matrix via photochemically initiated thiol-ene reaction. With this design, it was possible to achieve both the formation of a percolation network and strong interfacial interactions between the nanofiller and the NR matrix, which should improve the strength and modulus while

retaining the high ductility of the nanocomposites. The strong interfacial interaction between the NR matrix and the end-modified CNF was characterized by Fourier-transform infrared (FTIR) spectroscopy. The structural and mechanical properties of the nanocomposites were evaluated by scanning electron microscopy (SEM), dynamic mechanical analysis (DMA) and mechanical tensile tests.

2. Experimental sections

2.1 Materials

The natural rubber (NR) latex with 60 wt% solid content was supplied by Centrotrade Deutschland GmbH (Eschborn, Germany). Cellulose nanofibril (CNF) aqueous suspension (CNF, 3 wt%) was obtained from CTP (Centre Technique du Papier, Grenoble). It was isolated from strongly refined bleached birch pulp using an enzymatic pretreatment and a final homogenization step. 6-Amino-1-hexanethiol hydrochloride (AHH), 2-hydroxy-4-(2-hydroxyethoxy)-2-methylpropiophenone (Irgacure 2959), 1-[3-(dimethylamino)propyl]-3-ethylcarbodiimide methiodide (EDC), N-hydroxysuccinimide (NHS), sodium triacetoxyborohydride (Ac), and sodium chlorite ($NaClO_2$) were purchased from Sigma Aldrich. Potassium chloride (KCl), sodium carbonate anhydrous (Na_2CO_3), acetic acid, hydrochloric acid (HCl), silver nitrate ($AgNO_3$), sodium borohydride ($NaNH_4$), and sulfuric acid (H_2SO_4, 98%) were purchased from Roth and used as received.

2.2 CNF end modification by sodium triacetoxyborohydride and 6-Amino-1-hexanethiol hydrochloride via aldimine condensation

106 The pH of CNF aqueous dispersions (10 mg/mL) was regulated to 9.2 with Na_2CO_3
107 buffer solution in oil bath at 70°C. $NH_2(CH_2)_6SH{\cdot}HCl$ (0.3 mmol) and reducing agent
108 Ac (45 mmol) were dissolved in distilled water and added into the CNF suspension by
109 magnetic stirring under the protection of nitrogen for 3 days. After reaction, the
110 dispersion was cooled to room temperature. Then 20 mL of 3 M HCl solution was
111 added to neutralize the excess reducing agent (Ac), and the neutralized suspension
112 was dialyzed against distilled water for 5 days. Then the KCl solution was added
113 under magnetic stirring for 24h. After incubation treatment, the CNF-SH-a suspension
114 was obtained by dialysis against distilled water to remove electrolytes.

115 **2.3 CNF end modification by 6-Amino-1-hexanethiol hydrochloride, EDC, NHS**
116 **via carboxyamine condensation**

117 The end aldehyde groups of CNF were first converted into carboxyl groups (–COOH)
118 (Arcot, Lundahl, Rojas, & Laine, 2014). $NaClO_2$ solution (250 mM) was added to the
119 CNF aqueous suspension (10 mg mL^{-1}) at room temperature for 20 h, the pH of the
120 aqueous suspension was regulated to 3.5 by acetic acid, and it was followed by
121 dialysis against distilled water to remove excess reactants. The resulting CNF-COOH
122 suspension with carboxyl ends was used for further modification. The pH of the CNC-
123 COOH suspension (5 mg/mL) was adjusted to 7.0, then NHS (0.3 mmol) and EDC (3
124 mmol) were added under the protection of nitrogen. Following, the pH of the
125 suspension was adjusted to 6.5, and desired amounts of KCl (1 M) solution were
126 added to increase the ionic strength. Then the carboxyamine reaction started with the

addition of $NH_2(CH_2)_6SH \cdot HCl$ (3 mmol) under a pH of 9.2 (regulation by 0.1 M Na_2CO_3 buffer) at room temperature. After the 2 h incubation, the resulting CNF with end-thiol (CNF-SH-b) was obtained by dialysis against distilled water to remove the unreacted reagents.

2.4 Preparation of NR/CNF-x and NR/CNF-SH-x nanocomposites

The nanocomposites were prepared by mixing the two aqueous dispersions and casting/evaporating. The desired amount of pristine CNF or end-modified CNF-SH and NR latex was first mixed uniformly. Then the photoinitiator (Irgacure 2959, 2 wt%) was added into the mixture suspension under magnetic stirring for 3 h. Next, the uniform mixture suspension was exposed to UV irradiation (365 nm) to initiate the click reaction between NR matrix and CNF-SH under controlled intensity and distance for 30 min. Finally, the mixture suspension was poured into PTFE molds (diameter =100 cm) at 45°C overnight to get the nanocomposites by water evaporation. Two kinds of composites were prepared and codified as NR/CNF-x and NR/CNF-SH-x with various CNF or CNF-SH contents (x = 0, 2, 5, 8, 10, 15 wt %). The CNF and CNF-SH contents were based on the total solid content.

2.5 Characterization

Elemental analysis (EA) was performed to trace the content of nitrogen (N %) and sulfur (S %) elements after modification with elemental analyzer (Elemental Analysis system, GmbH). X-ray photoelectron spectroscopy (XPS) experiments were carried out on a Thermo Fisher spectrometer.

148 The Zeta potential of CNF and CNF-SH suspensions was measured with Zetasizer
149 Nano instrument (Malvern). Fourier-transform infrared spectroscopy (FTIR)
150 measurements were performed on a Perkin Elmer Spectrum 65 spectrometer in the
151 range 4000-600 cm^{-1}. Solid-state NMR analysis was performed on a Bruker AVANCE
152 400 NMR spectrometer with a 4 mm CP-MAS probe at 12 000 Hz spinning speed and
153 6 s relaxation delays. Thermogravimetric analysis (TGA) curves were recorded from
154 25°C to 600°C (10°C/min) under nitrogen atmosphere. X-ray diffraction (XRD)
155 (Bruker, Germany) was performed by Cu Kα radiation at 40 KV. The diffraction angle
156 (2θ) was varied from 5 to 45° with a rate of 0.02°/s. The Segal method was used to
157 calculate the crystallinity index from XRD data (Zhu, Xu, Dufresne, & Lin, 2018).
158 The CNF suspension was negatively stained with a 2 wt% uranyl acetate solution, and
159 samples were observed with a transmission electron microscope (JEOL JEM 2100-
160 Plus) at 200 kV. For the CNF-SH suspension, a silver-staining technique was used to
161 identify the reducing end modification by in situ growth method. The silver nitrate
162 solution (1 mL, 1 mM) was added to the CNF-SH suspension (10 mL, 1 mg mL^{-1})
163 under magnetic stirring for 30 min. Then sodium borohydride solution (10 mL, 5
164 mM) was added under magnetic stirring for 24h. The resulting suspension was
165 prepared for TEM.
166 The cross-linking density was determined as follows. Five weighed samples (m_0) were
167 each immersed in an airtight container of toluene at room temperature. The swollen
168 samples were then periodically taken out and immediately weighed on an analytical

169 balance (m_1) after wiping up with filter paper until a constant weight was obtained.

170 The cross-linking density (ν) was calculated by the Flory-Rehner equation (Flory &

171 Rehner, 1943; Jiang et al., 2021).

172 $$\nu = -\frac{\ln(1-V_{\mathrm{nr}})+V_{\mathrm{nr}}+xV_{\mathrm{nr}}^2}{V_{\mathrm{t}}\left(V_{\mathrm{nr}}^{1/3}-\frac{V_{\mathrm{nr}}}{2}\right)} \quad (1)$$

173 $$V_{\mathrm{nr}} = \frac{\frac{m_{\mathrm{nr}}}{\rho_{\mathrm{nr}}}}{\frac{m_{\mathrm{t}}}{\rho_{\mathrm{t}}}+\frac{m_{\mathrm{nr}}}{\rho_{\mathrm{nr}}}} \quad (2)$$

174 where x and V_t are the interaction parameter and molar volume of toluene (x = 0.39, V_t

175 = 106.2 cm^3/mol), respectively. m_{nr} and ρ_{nr} are the weight and density of natural

176 rubber (ρ_{nr} = 0.93 g/cm^3), respectively. m_t and ρ_t are the weight and density of toluene

177 (ρ_s = 0.865 g/cm^3), respectively.

178 The network structure constructed with CNF in the NR nanocomposites was

179 identified by scanning electron microscopy (SEM) (Quanta 200 FEI). The NR/CNF

180 nanocomposites were put in liquid nitrogen for a few minutes and fractured.

181 The mechanical properties of NR/CNF and NR/CNF-SH nanocomposites were

182 measured in tensile mode (Instron 5567, USA). The measurements were performed at

183 a strain rate of 100 mm/min. The sample dimensions were 18 × 6 × 0.6 mm^3, and the

184 results were averaged on five measurements. The toughness of the nanocomposites

185 was calculated from the area under the stress-strain curve before rupture.

186 Successive tensile tests were carried out to investigate the energy dissipation of

187 nanocomposites using Instron 5567. At the beginning of each experiment, the sample

188 was first stretched under a load of 0.5 N. Then, the experiment consisted in stretching

189 the sample up to a given elongation ΔL_1= 10 mm (cycle 1), then releasing the force
190 down to 0.5 N, and stretching again up to $\Delta L_2 = 2\Delta L_1$ (cycle 2). This procedure was
191 repeated with increasing elongation $\Delta L_i = i\Delta L_1$ until the rupture of the sample. The
192 tensile modulus E_i and the shrinkage r_i were determined for each successive cycle.
193 Dynamic mechanical analysis (DMA, TA, USA) was carried out from -100 to 100 °C
194 at 5 °C min^{-1} in tensile mode. The strain amplitude and frequency were 0.05% and 1
195 Hz, respectively.

196 ## 3. Results and discussion

197 The main objectives of this work were the preparation of reducing end modified CNF
198 and the development of nanocomposites by reactive compounding between reducing
199 end modified CNF and NR matrix. As shown in Scheme 1, the aim of the reducing
200 end modification was to introduce active thiol groups (−SH) at the reducing ends of
201 CNF, while being able to retain the surface hydroxyl groups (-OH). Subsequently,
202 covalently cross-linked nanocomposites were prepared by click reaction between the -
203 SH groups on the end modified CNF-SH and unsaturated bonds (-C=C-) of the NR
204 matrix via UV radiation.

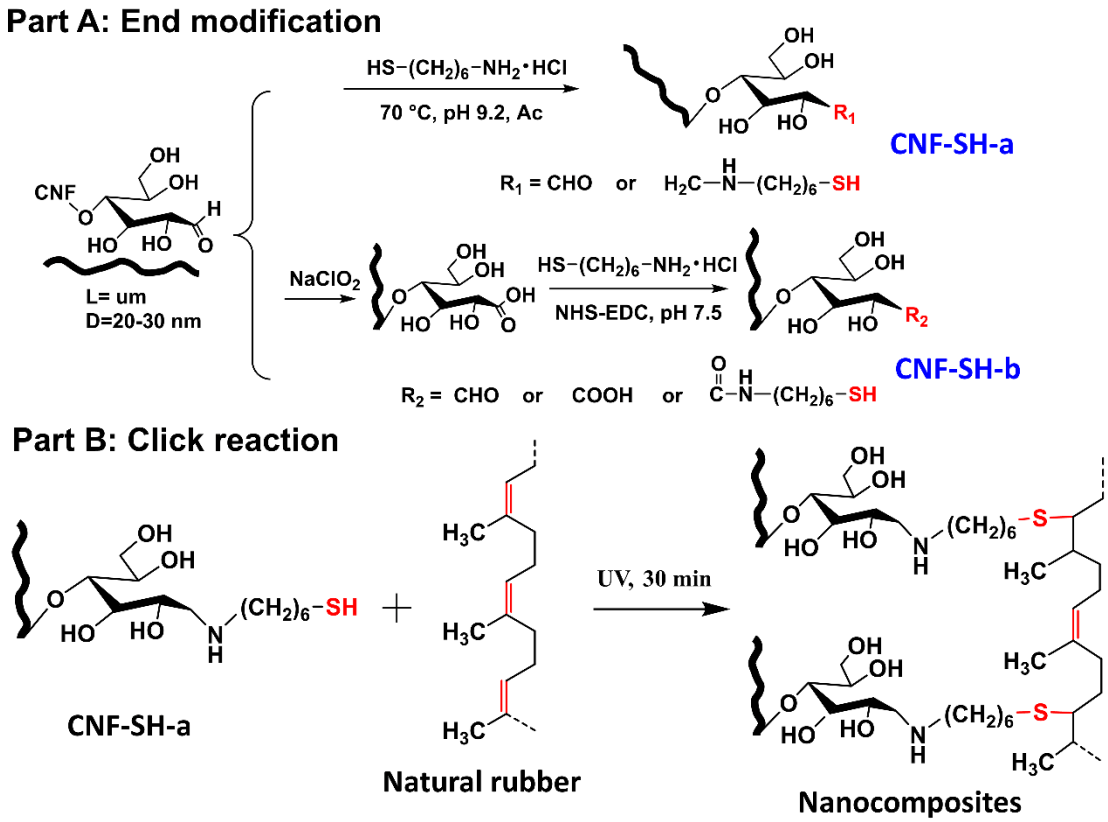

Scheme 1 Reducing end modification of CNF and preparation of nanocomposites.

3.1 Analysis of reducing end modification of CNF

In this study, two strategies were designed to achieve end modification of CNF, including aldimine condensation (CNF-SH-a) and carboxyamine condensation (CNF-SH-b), as shown in Scheme 1 (Part A). For the chemical reaction mechanism of CNF-SH-a, the active end aldehyde groups were easily nucleophilically attacked by the primary amino group, inducing aldimine condensation. This reaction initially formed a covalent linkage through the generation of an unstable -C=N- group, which was then reduced by Ac to form a stable -C-N- group, resulting in the CNF-SH-a terminal modification. Regarding the chemical reaction mechanism for CNF-SH-b, the CNF end aldehyde group was oxidized to carboxyl group by $NaClO_2$ solution, and then

combined with EDC catalyst to form O-acylisourea active intermediate, which was converted into active NHS-CNF-ester product under NHS catalysis. Finally, the nucleophilic attack by the primary amino group and the cleavage of NHS-CNF-ester occurred to obtain end modified CNF-SH-b.

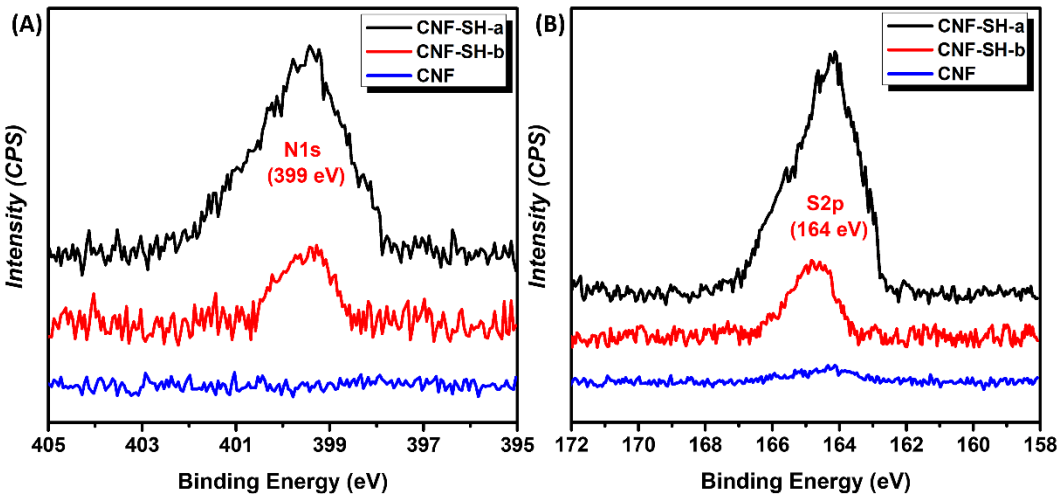

Fig. 1 XPS spectra for CNF, CNF-SH-a and CNF-SH-b: (A) N1s and (B) S2p spectra.

Compared to surface modifications, the end modification of CNF has relatively few active sites. XPS and elemental analysis were used to track the changes in sulfur and nitrogen elements. As shown in Fig. S1, the typical characteristic signals of O1s (534 eV) and C1s (287 eV) can be observed in the XPS spectrum for CNF before and after end modification. At the same time, characteristic peaks of N1s (399 eV) and S2p (164 eV) were observed in the end-modified CNF-SH spectrum, which is consistent with the results of elemental analysis (Table S1), which proved that the thiol group (-SH) was successfully grafted to the reducing end of CNF. It is worth noting that elemental analysis results show that the nitrogen and sulfur content in CNF-SH-a was higher than that of CNF-SH-b; the peak intensity for N1s and S2p for CNF-SH-a in

the XPS characteristic element spectrum was also stronger than that of CNF-SH-b (Fig. 1A and 1B), indicating that CNF-SH-a has a higher grafting efficiency than CNF-SH-b.

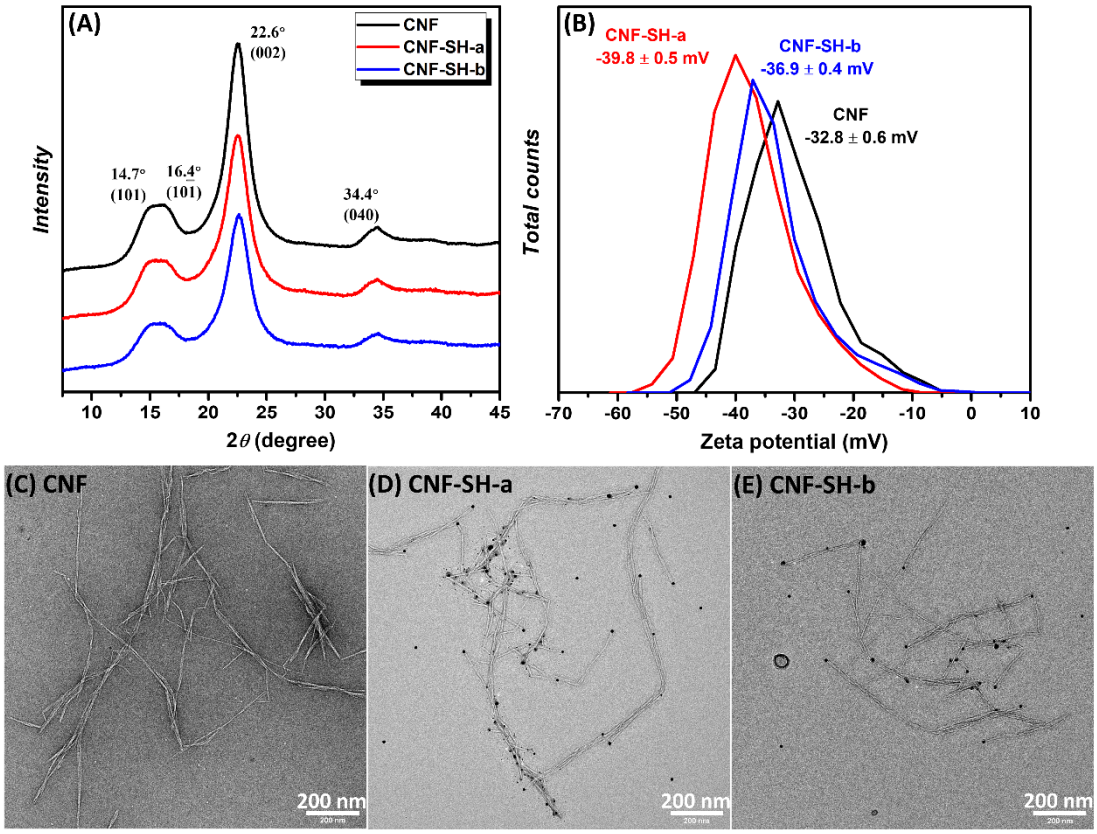

Fig. 2 (A) XRD spectrum and (B) Zeta potential for CNF before and after modification; TEM images for (C) pristine CNF, negatively silver nanoparticle-stained (D) CNF-SH-a and (E) CNF-SH-b.

The crystalline properties and zeta potential value for CNF before and after end modification were investigated. As shown in Fig. 2A, the XRD pattern for pristine CNF and modified CNF (CNF-SH-a and CNF-SH-b) showed typical cellulose I crystalline characteristic peaks. According to Segal formula (Zhu, Chen, Wu, & Lin, 2019), the crystalline index for pristine CNF, CNF-SH-a and CNF-SH-b was 72.8%,

66.8% and 65.7%, respectively, which indicates that the end modification process did not significantly impair the original crystalline structure of CNF. Zeta potential measurements were used to prove the stability of the suspension before and after modification. It is considered that a zeta potential value lower than -30 or over 30 mV provides adequate repulsive force to achieve colloidal physical stability (Joseph & Singhvi, 2019). As shown in Fig. 2B, end-modified CNF-SH-a and CNF-SH-b maintained a high zeta potential absolute value (-39.8 mV and -36.9 mV, respectively), which shows its good dispersibility ability.

After end modification, sulfur atoms were successfully grafted on the reducing end of CNF. According to the well-known spontaneous reaction between silver nanoparticles and sulfur, the regioselective labeling of CNF-SH with silver nanoparticles via a σ-π coordinate bond (Ning, Xie, Xing, Deng, & Yang, 1996; Ulman, 1996) could prove the reducing end modification. As shown in Fig. 2C-E, CNF, CNF-SH-a and CNF-SH-b maintained a fibrous morphology and good dispersibility, as expected from zeta potential measurements. Furthermore, most of CNF-SH were labeled with several silver nanoparticles located on one end of CNF-SH by the in-situ growth strategy. These results provide visual evidence of the successful modification of the reducing end of CNF. In agreement with XPS and EA results, it was observed that the amount of silver nanoparticles labeling on CNF-SH-a is significantly higher than for CNF-SH-b, indicating that the grafting efficiency of the former is higher than the latter.

3.2 Click reaction between CNF-SH-a and NR

End-modified CNF-SH-a with -SH groups could react with the unsaturated double bond (-C=C-) of NR matrix under UV radiation to achieve a reactive compound. To demonstrate the chemical reaction between CNF-SH-a and NR matrix, the reaction mixture consisting of NR matrix and CNF-SH-a (2:1 w/w) was purified after 30 min of UV radiation under stirring. The mixture was prepared by continuous centrifugation and washing with acetone to completely remove unreacted NR component and the purified product was conditioned at 40°C in an oven overnight. For comparison, purified NR/CNF was also subjected to the same treatment.

As shown in Fig. 3A, compared to the FTIR spectra of pristine NR and CNF, the purified NR/CNF-SH-a mixture exhibits an out-of-plane bending vibrational peak assigned to =C–H for the alkene group on NR matrix at 836 cm^{-1} (Neto et al., 2016). However, the FTIR spectrum for the purified NR/CNF mixture was essentially identical to pristine CNF with no new peak appearing. Furthermore, the characteristic peaks were observed in the solid-state NMR spectrum of purified NR/CNF-SH-a mixture, corresponding to C1' (33ppm), C4' (27ppm) and C5' (23ppm) in the chemical structure of isoprene (Kawahara, Chaikumpollert, Sakurai, Yamamoto, & Akabori, 2009). Combining FTIR and ^{13}C ssNMR results, it is shown that the covalent bond formed by the click reaction between the end-modified CNF-SH-a and NR corresponds to a strong interaction, so that successive centrifugation and washing steps cannot remove the NR component covalently bonded to CNF-SH-a, and the characteristic peaks belonging to NR were observed in the FTIR and ssNMR spectra

of the purified NR/CNF-SH-a mixture. The interaction between NR and unmodified CNF is weak in the NR/CNF mixture and therefore the free NR component can be easily removed during the purification process.

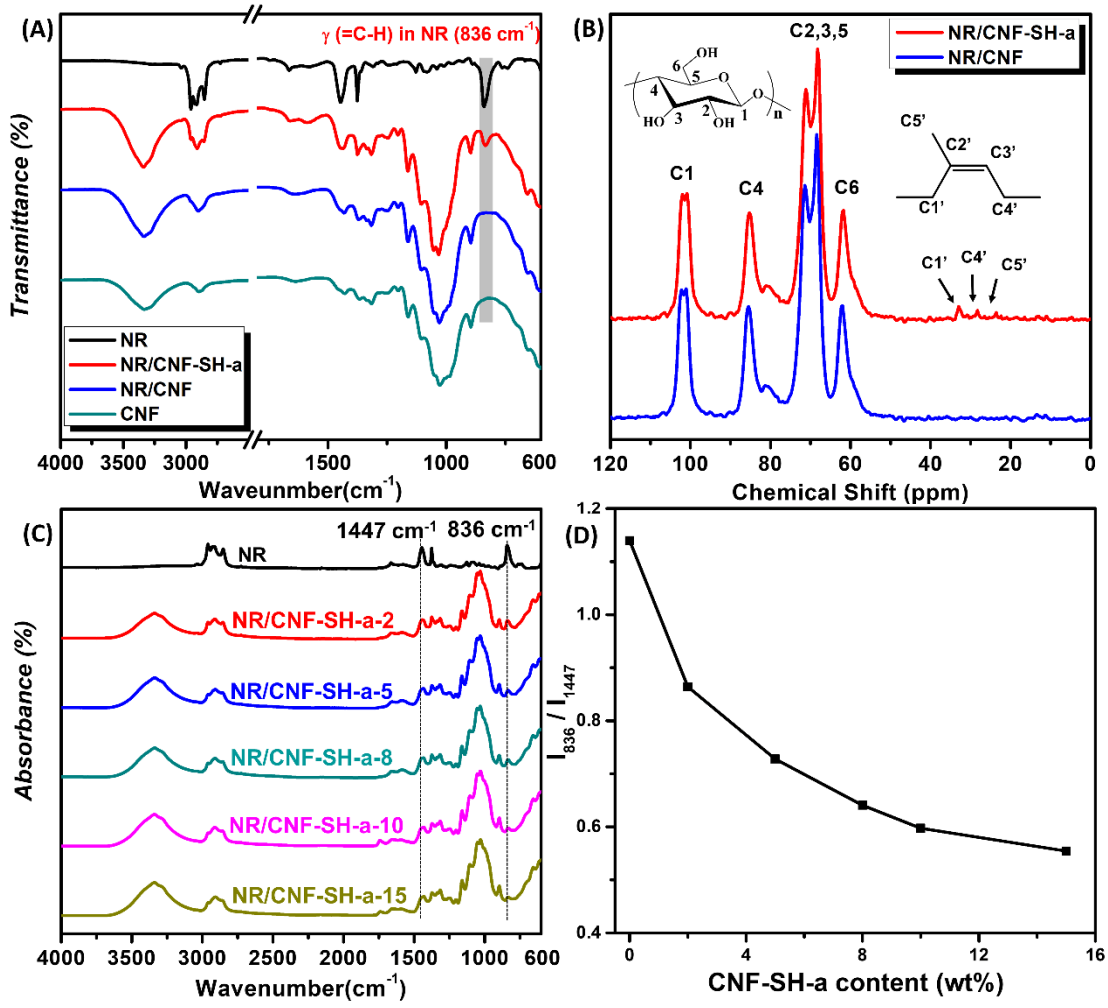

Fig. 3 (A) FTIR spectra for NR, NR/CNF-SH-a (2:1 w/w), NR/CNF (2:1 w/w) and pristine CNF; (B) ^{13}C solid-state NMR spectra for NR/CNF-SH-a (2:1 w/w) and NR/CNF (2:1 w/w). (C) FTIR spectra for the nanocomposites with different CNF-SH-a contents; (D) Evolution of I_{836}/I_{1447} as a function of CNF-SH-a content.

The interfacial interaction between CNF-SH-a and NR matrix in the nanocomposites was investigated by FTIR, as shown in Fig. 3C. The peak at 836 cm^{-1} was assigned to

297 the =C-H out-of-plane bending vibration of the alkene group. Compared to neat NR,
298 the intensity of the peak at 836 cm^{-1} for the nanocomposites decreased when
299 increasing the CNF-SH-a content, attributed to the click reaction between the double
300 bond in the NR chain and the -SH group of CNF-SH-a. To further explore the
301 chemical reaction between CNF-SH-a and NR matrix, the C-H bending vibration of
302 the methyl group at 1447 cm^{-1} was chosen as a comparison to normalize the intensity
303 of the =C-H peak at 836 cm^{-1} by integrating the area of the two peaks in the spectra of
304 the nanocomposites (I_{836}/I_{1447}). The I_{836}/I_{1447} value decreased from 1.14 to 0.55, when
305 increasing the CNF-SH-a content from 0 to 15 wt%, as shown in Fig. 3D. These
306 results demonstrate that covalent bonds are formed and controlled between the thiol
307 group of CNF-SH-a and the unsaturated double bond in the NR matrix.

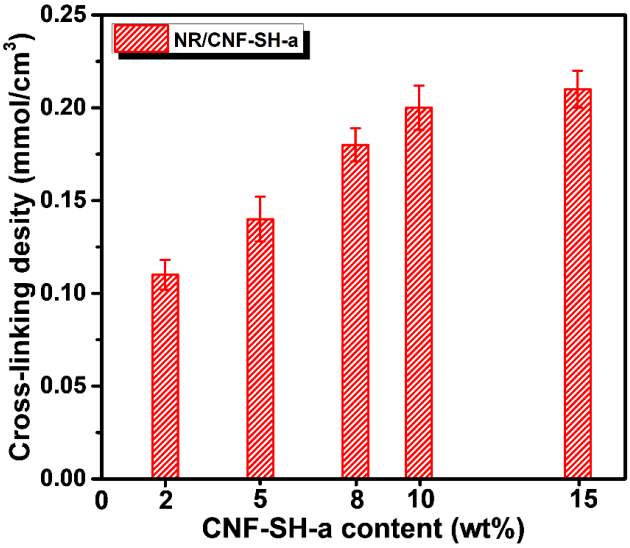

308
309 **Fig. 4** Cross-linking density of the nanocomposites with different CNF-SH-a contents.
310 The cross-linking density was calculated by the solvent swelling measurement method
311 using the Flory-Rehner equation. As shown in Fig. 4, The cross-linking density of

312 NR/CNF-SH-a-x nanocomposites increases when increasing the CNF-SH-a content,
313 which is consistent with the results of FTIR analysis. Compared with NR/CNF-SH-a-
314 2 (0.11 mmol/cm^3), NR/CNF-SH-a-15 nanocomposite exhibits a higher cross-linking
315 density (0.21 mmol/cm^3). The results indicate that the improvement of interfacial
316 interaction in the nanocomposites may contribute to increase the cross-linking density.
317 The strong interfacial interaction between CNF-SH-a and NR matrix through click
318 chemistry resulted in a tight bond between the filler and the matrix, effectively
319 binding the polymer chains together. The greatly increased proportion of rigid phase
320 in the matrix (Tang & Weder, 2010) slows down the penetration of the solvent into
321 the matrix, thereby reducing the solvent adsorption and swelling of the NR/CNF-SH-a
322 nanocomposites.

323 **3.3 Morphology of ENR/CNs nanocomposites**

324 The fractured surface for neat NR and nanocomposites reinforced with 5 wt% CNF-
325 SH-a or CNF were observed by SEM to evaluate the compatibility between the filler
326 and NR matrix. As shown in Fig. 5 (A and D), a smooth and uniform morphology was
327 observed for unfilled NR. CNF-SH-a was homogeneously dispersed in the NR matrix
328 without significant aggregation (Fig. 5B and 5E) due to the introduction of relatively
329 long NR chains at the end of CNF-SH-a via click reaction, which weakened the
330 hydrophilic character and hydrogen-bonding tendency of CNF-SH-a. Furthermore, no
331 gaps or voids were found in the NR/CNF-SH-a-5 nanocomposites, indicating good
332 interfacial compatibility between CNF-SH-a and NR matrix. The good interfacial

compatibility was mainly attributed to the strong interaction between CNF-SH-a and NR matrix via click reaction. However, a significant micro-phase separation (two layers: one rougher phase and another smoother phase) was observed for NR/CNF-5 nanocomposites. The rougher phase possibly corresponded to the aggregation of unmodified CNF at the bottom of the PTFE molds during water evaporation. The simple physical compounding of hydrophilic CNF and hydrophobic NR matrix resulted in poor interfacial compatibility and significant micro-phase separation for the NR/CNF-5 nanocomposite. Therefore, the good interfacial compatibility for CNF-SH-a reinforced materials is expected to greatly improve the properties of the resulting nanocomposites (Cao, Yuan, Fu, & Chen, 2018).

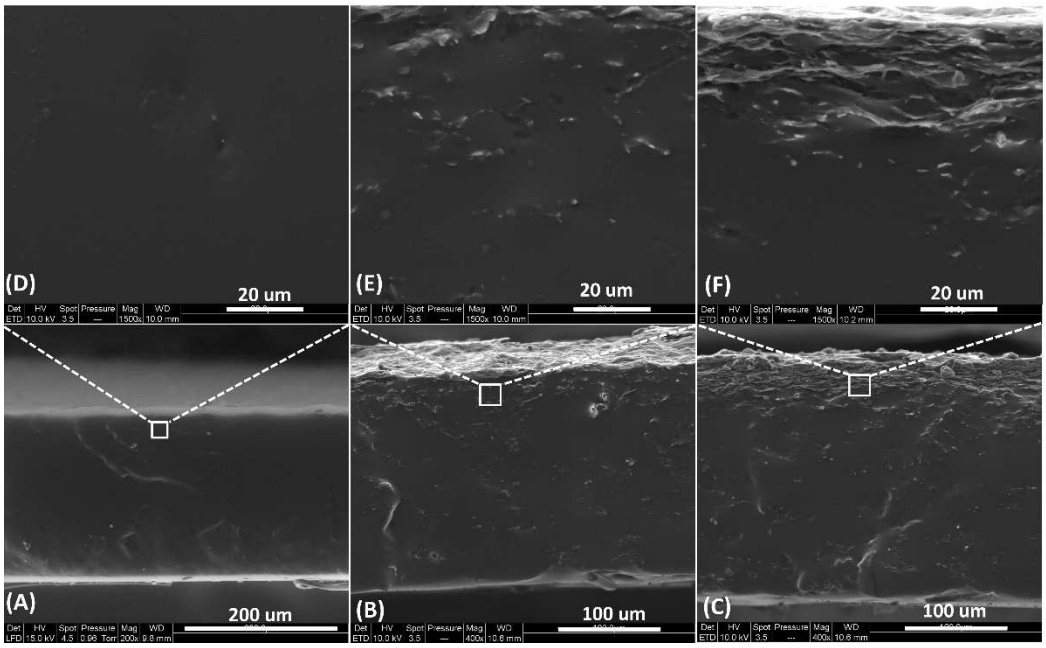

Fig. 5 SEM of fractured surfaces for (A, D) neat NR, (B, E) NR/CNF-SH-a-5 and (C, F) NR/CNF-5 with different magnifications. The regions delimited by white rectangles in (A, B and C) images correspond to the lower face of the composite films, which are in contact with the PTFE mold during water evaporation.

3.4 Mechanical properties of nanocomposites

The mechanical properties of NR/CNF and NR/CNF-SH-a nanocomposites were characterized by tensile tests. Typical stress-strain curves for the nanocomposites and pure NR are shown in Fig. 6, and the tensile properties are collected in Table S2. Compared to neat NR, the modulus and tensile strength of the nanocomposites increased significantly with the addition of CNF and CNF-SH-a. The tensile strength for NR/CNF-SH-a-10 (5.83 MPa) was 17.6 times higher than that of neat NR (0.33 MPa) and 1.67 times higher than that of NR/CNF-SH-10 (3.48 MPa). Meanwhile, the Young's modulus for NR/CNF-SH-a-10 (45.25 MPa) was 94.3 times higher than that of neat NR (0.48 MPa) and 1.27 times higher than that of NR/CNF-SH-10 (35.55 MPa). The elongation at break of the nanocomposites decreased when increasing the CNF and CNF-SH content, in line with previous studies (Cao et al., 2013; Cao, Xu, Liu, & Chen, 2013). This is mainly attributed to the fact that the entangled CNF network expected to form within the NR matrix provides higher stiffness at the expense of ductility. Meanwhile, the strong interfacial interaction between NR and CNF-SH via click reaction held the matrix and filler more tightly and restricted the movement of NR chain segments. The toughness of the nanocomposites increased when increasing CNF and CNF-SH-a content. For 15% CNF content, the toughness decreased due to the aggregation of CNF in the NR matrix, which is consistent with SEM observations. The toughness of NR/CNF-SH-a-10 (22.24 MJ m^{-3}) was 8.45 times higher than that of neat NR (2.63 MJ m^{-3}) and 1.78 times higher than that of

NR/CNF-SH-10 (12.51 MJ m^{-3}). Therefore, for a given CNF content, a lower degradation of the ductility of the material is observed for CNF-SH-a based nanocomposites. These results indicate the synergistic effect of the rigid CNF-SH-a reinforcement together with cross-linking at the filler-matrix interface.

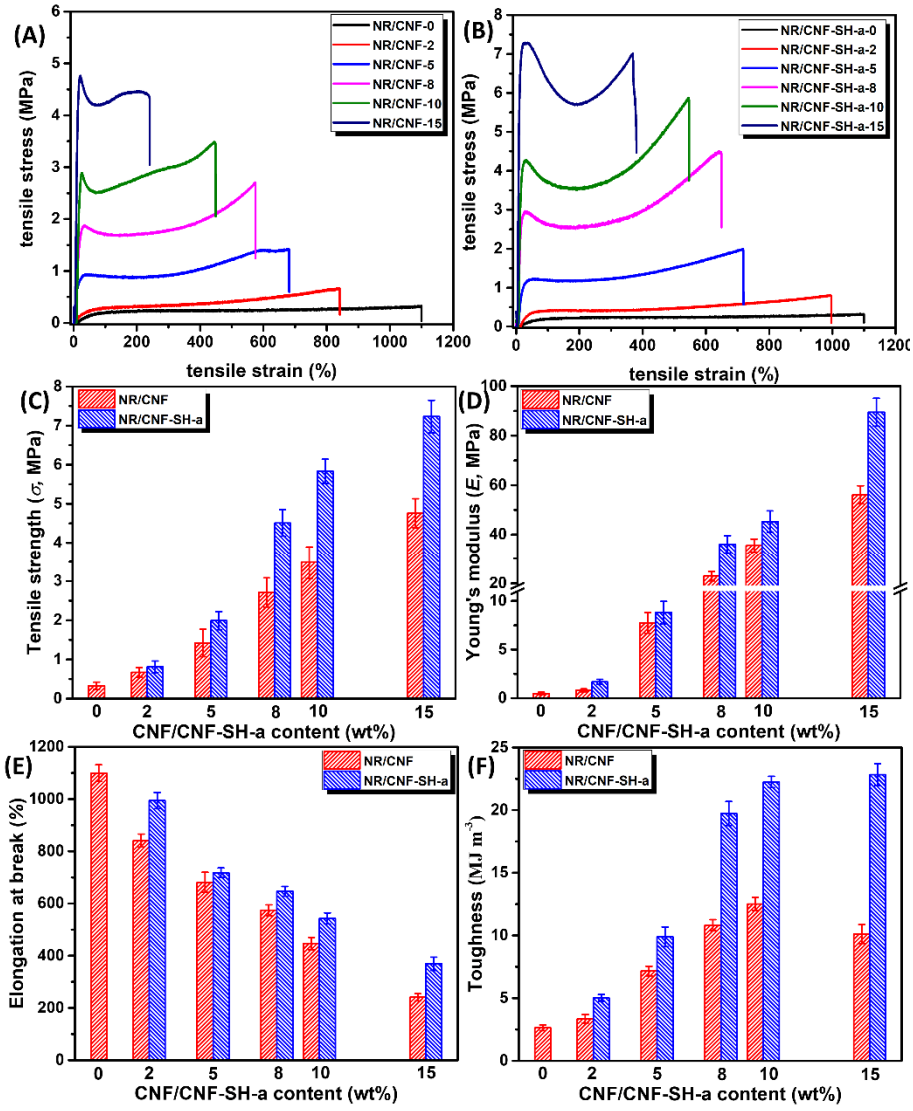

Fig. 6 Stress-strain curves for (A) NR/CNF nanocomposites, and (B) NR/CNF-SH-a nanocomposites. Evolution of (C) the tensile strength, (D) Young's modulus, (E) elongation at break and (F) toughness as a function of filler content for neat NR and nanocomposites (the error bars are standard deviations).

3.5 Successive tensile tests

The stress-strain curves obtained from the successive tensile tests applied to the nanocomposites are shown in Fig. 7A and 7B. During the successive tensile tests, the positive stretch curve and the negative recovery curve were not superimposed. Meanwhile, a residual elongation was induced for each cycle, which is due to the entropic nature of the strain and the involvement of the viscoelastic component to the total compliance. It is worth noting that it is mainly influenced by the experimental stretching rate and temperature, and it is strongly time-dependent (Angellier, Molina-Boisseau, & Dufresne, 2005; Bendahou, Kaddami, & Dufresne, 2010). For subsequent cycles, the nanocomposites could be stretched to an elongation above their elastic limit, since the rubber was unvulcanized.

The shrinkage r_i of the nanocomposites was determined by the difference between the elongation and the residual elongation retained at the end of each cycle. The evolution of the tensile modulus E_i and shrinkage r_i during the successive cycles is plotted in three-dimensional diagram (Fig. 7C and 7D, respectively). For all samples, the tensile modulus showed a continuous decreasing trend during successive cycles, where the higher the nanocellulose contents was, the stronger the modulus drop was, as shown in Table S3. During the first successive tensile tests, the decrease in modulus of the nanocomposites could be attributed to the gradual breakdown of the continuous nanocellulose network. We also observed that the tensile modulus of the nanocomposites was higher than that of neat NR for a given cycle, while the modulus

399 increased with increasing nanocellulose content, which is consistent with tensile test
400 results, as well as DMA experiments that will be reported latter.
401 Regardless of the sample, residual elongation was observed from the first stretching
402 cycle, while shrinkage increases during successive tensile tests. These data suggest
403 that the viscous flow in the samples decreases for each successive stretching cycle,
404 while the elastic recovery component increases. For a given cycle, the shrinkage of
405 the nanocomposites was lower than that of the neat NR matrix. In addition, the
406 nanocomposites reinforced with CNF-SH-a exhibit higher shrinkage than that of CNF
407 in a given cycle. This indicated that CNF-SH-a induces a more elastic behavior of the
408 nanocomposite while reducing its viscoelasticity, demonstrating the interaction
409 between CNF-SH-a and NR matrix.

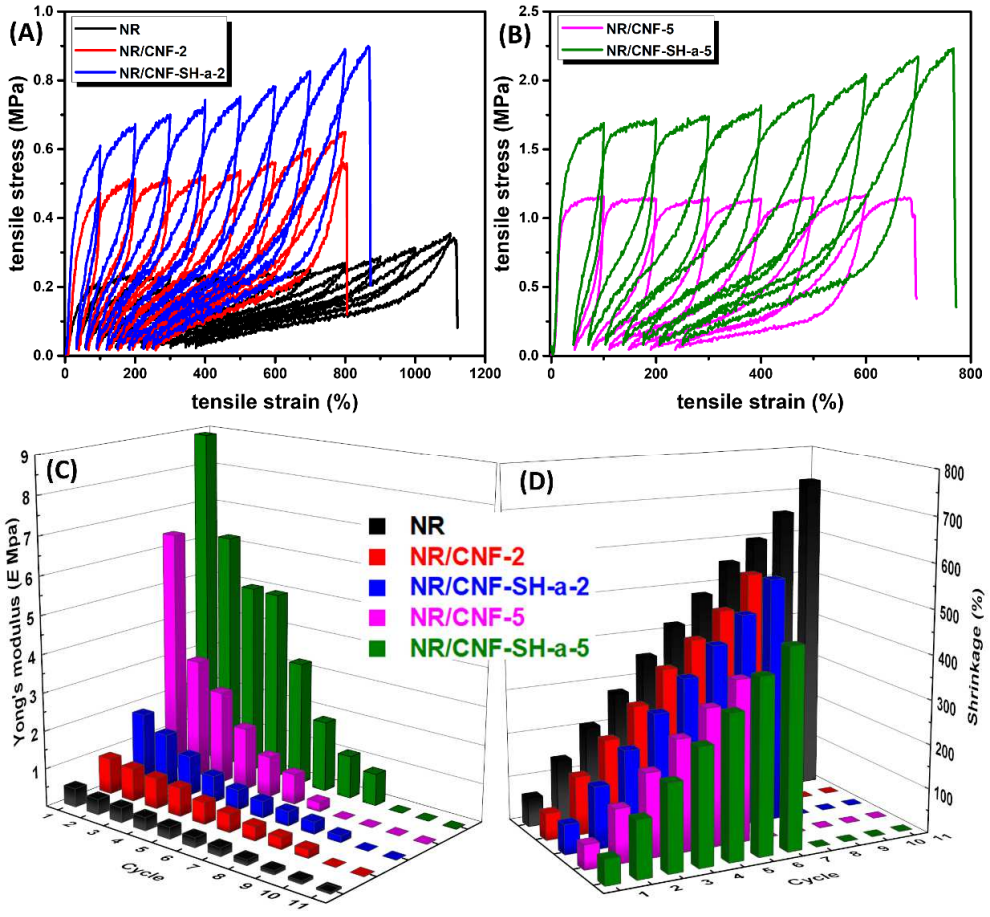

410

411 **Fig. 7** Stress-strain curves recorded during successive tensile tests for (A) NR,
412 NR/CNF-2, and NR/CNF-SH-a-2 nanocomposites; (B) NR/CNF-5, NR/CNF-SH-a-5
413 nanocomposites; and evolution of (C) the tensile modulus E_i and (D) the shrinkage
414 r_i measured during each cycle i for NR/CNF and NR/CNF-SH-a nanocomposites.

415 **3.6 Dynamic mechanical analysis**

416 Typical dynamic mechanical curves for the isochronal evolution of the tensile storage
417 modulus (E') and loss factor (tan δ) as a function of temperature for pure NR,
418 NR/CNF-5, NR/CNF-10, NR/CNF-SH-a-5 and NR/CNF-SH-a-10 nanocomposites
419 are shown in Fig. 8. At low temperature, E' remains roughly constant around 3 GPa
420 (Fig. 8A). It is due to the fact that in the glassy state, molecular motions are largely
421 restricted to vibration and short-range rotational motions. Increasing the CNF content

successively increased the E' value. This sort of modulus enhancement, even below the glass transition temperature, is good evidence for the strong reinforcing tendency of CNF in the NR matrix. A sharp modulus drop over about three decades is observed for all samples around -55°C, which corresponds to the relaxation process associated to the glass transition of the NR matrix. This modulus drop is linked to an energy dissipation phenomenon displayed through the concomitant increase of the loss factor where tan δ passes through a maximum (Fig. 8B). This relaxation process involves cooperative motions of long chain sequences. Above T_g, the modulus becomes roughly constant and corresponds to the rubbery modulus. In this temperature range, the impact of the filler on the stiffness of the material appears more distinctly, due to the greater difference in the modulus of the two components. A higher reinforcing effect is observed for CNF-SH-a based nanocomposites compared to CNF based nanocomposites, probably because of stronger interactions between the filler and the matrix via click reaction, which increased the effective volume fraction of the rigid phase and led to the formation of a bound matrix material around the filler.

Compared to neat NR, the T_g of both nanocomposite materials showed a slight shift towards higher temperatures, as shown in Fig. 8B. Tan δ for neat NR exhibits a maximum at -56.4 °C, while it is -54.3 °C and -51.5 °C for NR/CNF-10 and NR/CNF-SH-a-10 nanocomposites, respectively. This is mainly attributed to the restricted segmental movement due to strong interaction between the filler and the matrix. Meanwhile, the increased cross-linking density also led to an increase of T_g.

As the filler content increased, the magnitude of the damping peak associated to the glass transition for both nanocomposites decreased, probably due to the covalent bonds formed between the filler and the NR chain segment molecules, which greatly restricted the movement of the NR chains. These results suggest that strong covalent links exist at the composite interface for NR/CNF-SH-a nanocomposites, while a denser cross-linked NR network would give a stronger reinforcement effect of CNF-SH-a in the rubbery state.

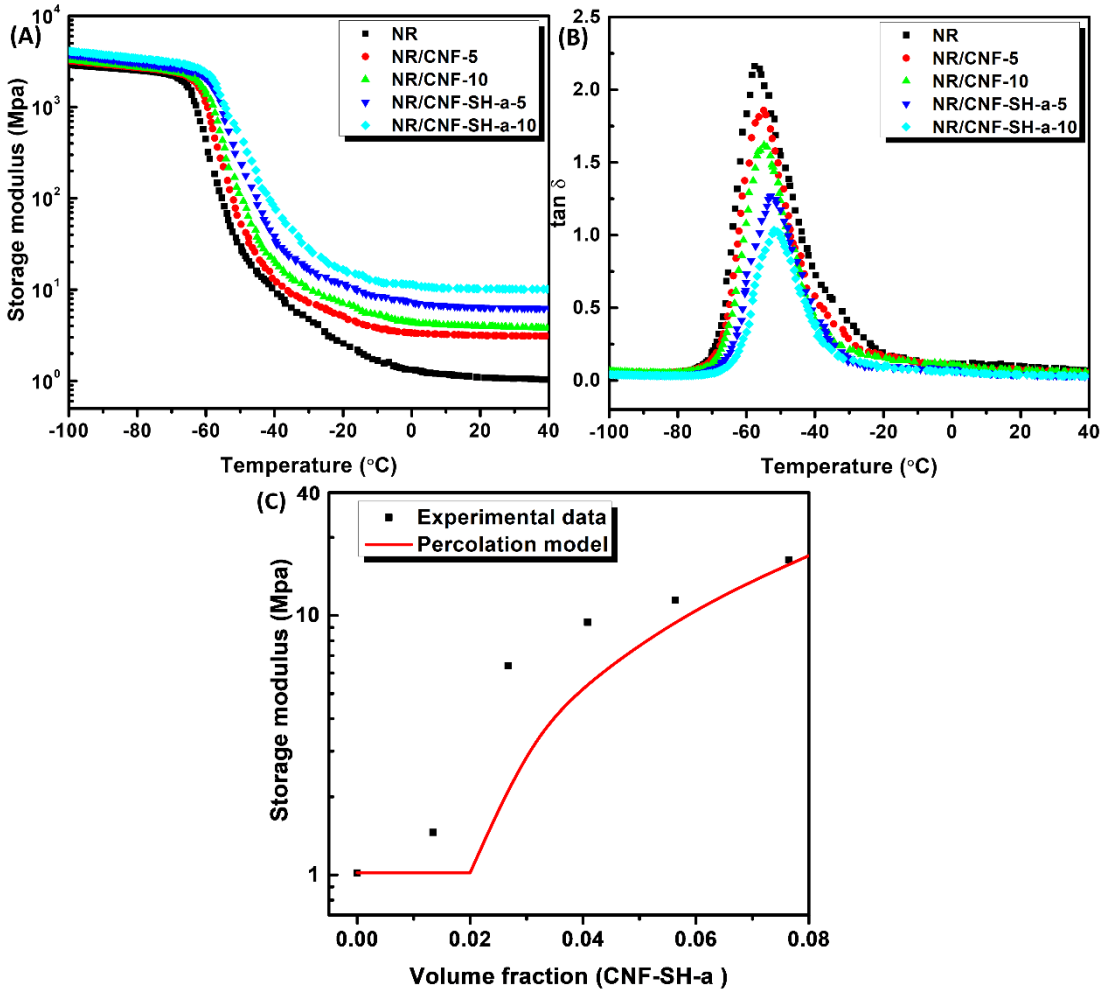

Fig. 8 Typical dynamic mechanical analysis isochronal curves: (A) tensile storage modulus (E') and (B) loss factor (tan δ) vs. temperature for neat NR, NR/CNF-5, NR/CNF-10, NR/CNF-SH-a-5 and NR/CNF-SH-a-10 nanocomposites. (C) Evolution

454 of the predicted and experimental modulus for CNF-SH-a nanocomposites vs. CNF-
455 SH-a volume fraction at 25°C.

456 This high reinforcement effect could be attributed to the formation of a continuous
457 rigid three-dimensional percolation network structure by hydrogen bonds, which has
458 been extensively discussed in the literature and is well predicted by the percolation
459 approach adapted to the Takayanagi model (Azizi Samir, Alloin, & Dufresne, 2005;
460 Bras et al., 2010).

461 $$E' = \frac{(1-2\psi+\psi X_r)\mathrm{E}'_r E'_s+(1-\psi X_r)\psi {E'_r}^2}{(1-X_r)\mathrm{E}'_r+(X_r-\psi)E'_s} \quad (3)$$

462 $$\psi = X_r\left(\frac{X_r-X_c}{1-X_c}\right)^{0.4} \quad (4)$$

463 $$X_c = \frac{0.7}{f} \quad (5)$$

464 where E'_{r} is the storage modulus of the rigid filler network; E'_s is the storage modulus
465 of neat NR; X_r is the volume fraction of CNF-SH-a in the nanocomposite; X_c is the
466 volume fraction of CNF-SH-a at the percolation threshold; ψ is the volume fraction of
467 CNF-SH-a contributing to the percolation network; f is the aspect ratio of CNF-SH-a,
468 which was estimated to 34.8 according to TEM observations by software of
469 NanoScope Analysis 1.5. The density of NR and CNF-SH-a was 0.96 and 1.5 g cm^{-3},
470 respectively.

471 The comparison between predicted and experimental modulus it classically used to
472 evaluate the dispersion state of the filler within the polymer matrix and the formation
473 of a percolating network in the nanocomposite. At sufficiently high temperatures, i.e.
474 above *T*g of the NR matrix, the modulus of the percolating CNF-SH-a network (0.65

GPa) (Shanmuganathan, Capadona, Rowan, & Weder, 2010; Capadona et al., 2007) is much higher than that of the NR matrix (1.02 MPa, according to DMA results). Thus, Eq. 3 can be simplified and the storage modulus of the nanocomposite is just the product of the volume fraction of CNF-SH-a contributing to the percolation network (ψ) and modulus of the percolation rigid CNF-SH-a network (Dufresne, 2017; Bettaieb, Khiari, Dufresne, Mhenni, & Belgacem, 2015).

$$E' = \psi * E'_r \qquad (6)$$

Based on the above equation, the calculated percolation threshold of CNF-SH-a was 2.01 vol%, which is around 3.1 wt%. From Fig. 8C and Table S4 (in Supporting Information), it is obvious that for the nanocomposite reinforced with 5 wt% CNF-SH-a percolating network effectively formed. The end-modification allows CNFs to not only retain the original crystal structure and size, but also preserves the surface hydroxyl group, which serve as the driving force for hydrogen bonding and are the basis for rigid network formation (Fox, Capadona, Marasco, & Rowan, 2013). It significantly improved the dispersion and storage modulus of the nanocomposite.

4. Conclusions

We have demonstrated a novel concept for the development of rubbery nanocomposites based on the synergistic effect of cellulose nanofibrils used as a biobased reinforcement, which also possess cross-linking sites for covalent coupling to the natural rubber elastomer matrix. Reducing end-modified CNFs bearing -SH groups (CNF-SH-a) were successfully prepared by aldimine condensation at one end

of CNF with 6-Amino-1-hexanethiol hydrochloride. CNF-SH-a showed improved hydrophobicity and good dispersibility in hydrophobic medium. Nanocomposite films with homogeneous dispersion of CNF-SH-a in NR matrix were prepared by a casting/evaporating method. The cross-link density of the NR/CNF-SH-a sample was confirmed to significantly increase when increasing CNF-SH-a content. This is due to the covalent cross-links formed at the filler-matrix interface photochemically initiated by thiol-ene reaction. The NR nanocomposite reinforced with 10 wt%/CNF-SH-a showed significantly higher values of tensile strength (from 0.33 MPa to 5.83 MPa), Young's modulus (from 0.48 MPa to 45.25 MPa) and toughness (from 2.63 MJ m^{-3} to 22.24 MJ m^{-3}) compared to neat NR nanocomposites. As the present concept is general in material synthesis and design, we foresee that this green method to reinforce NR matrix with end-modified CNF-SH will have the potential application in textile, printing, automobile and machinery manufacturing fields.

Conflicts of interest

None.

Acknowledgements

This work was supported by the China Scholarship Council (CSC) under Grant No. 201806950016. LGP2 is part of the LabEx Tec 21 (Investissements d'Avenir—Grant Agreement No. ANR-11-LABX-0030) and of the PolyNat Carnot Institute (Investissements d'Avenir—Grant Agreement No. ANR-16-CARN-0025-01).

References

517 Angellier, H., Molina-Boisseau, S., & Dufresne, A. (2005). Mechanical properties of
518 waxy maize starch nanocrystal reinforced natural rubber. Macromolecules, 38, 9161-
519 9170.

520 Arcot, L., Lundahl, M., Rojas, O. J., & Laine, J. (2014). Asymmetric cellulose
521 nanocrystals: thiolation of reducing end groups via NHS–EDC coupling. Cellulose,
522 21, 4209-4218.

523 Azizi Samir, M. A. S., Alloin, F., & Dufresne, A. (2005). Review of recent research
524 into cellulosic whiskers, their properties and their application in nanocomposite field.
525 Biomacromolecules, 6, 612-626.

526 Bendahou, A., Kaddami, H., & Dufresne, A. (2010). Investigation on the effect of
527 cellulosic nanoparticles' morphology on the properties of natural rubber based
528 nanocomposites. European Polymer Journal, 46, 609-620.

529 Bettaieb, F., Khiari, R., Dufresne, A., Mhenni, M. F., & Belgacem, M. N. (2015).
530 Mechanical and thermal properties of Posidonia oceanica cellulose nanocrystal
531 reinforced polymer. Carbohydrate Polymers, 123, 99-104.

532 Bras, J., Hassan, M. L., Bruzesse, C., Hassan, E. A., El-Wakil, N. A., & Dufresne, A.
533 (2010). Mechanical, barrier, and biodegradability properties of bagasse cellulose
534 whiskers reinforced natural rubber nanocomposites. Industrial Crops & Products, 32,
535 627-633.

536 Cao, J., Zhang, X., Lu, C., Luo, Y., & Zhang, X. (2017). Self-healing sensors based
537 on dual noncovalent network elastomer for human motion monitoring
538 Macromolecular Rapid Communications, 38, 1700406.

539 Cao, L., Huang, J., & Chen, Y. (2018). Dual cross-linked epoxidized natural rubber
540 reinforced by tunicate cellulose nanocrystals with improved strength and extensibility.
541 ACS Sustainable Chemistry & Engineering, 6, 14802-14811.

542 Cao, L., Fan, J., Huang, J., & Chen, Y. (2019). A robust and stretchable cross-linked

543 rubber network with recyclable and self-healable capabilities based on dynamic
544 covalent bonds. Journal of Materials Chemistry A, 7, 4922-4933.

545 Cao, X., Xu, C., Wang, Y., Liu, Y., Liu, Y., & Chen, Y. (2013). New nanocomposite
546 materials reinforced with cellulose nanocrystals in nitrile rubber. Polymer Testing, 32,
547 819-826.

548 Cao, X., Xu, C., Liu, Y., & Chen, Y. (2013). Preparation and properties of
549 carboxylated styrene-butadiene rubber/cellulose nanocrystals composites.
550 Carbohydrate Polymers, 92, 69-76.

551 Capadona, J. R., Van Den Berg, O., Capadona, L. A., Schroeter, M., Rowan, S. J.,
552 Tyler, D. J., & Weder, C. (2007). A versatile approach for the processing of polymer
553 nanocomposites with self-assembled nanofibre templates. Nature Nanotechnology, 2,
554 765-769.

555 Chen, Y., Huang, X., Gong, Z., Xu, C., & Mou, W. (2017). Fabrication of high
556 performance magnetic rubber from NBR and Fe_3O_4 via in situ compatibilization with
557 zinc dimethacrylate. Industrial & Engineering Chemistry Research, 56, 183-190.

558 Dufresne, A. (2017). *Nanocellulose: from nature to high performance tailored*
559 *materials*. (2nd ed.) Walter de Gruyter GmbH & Co KG.

560 Flory, J. & Rehner Jr, J. (1943). Statistical mechanics of cross-linked polymer
561 networks I. Rubberlike elasticity. The Journal of Chemical Physics, 11, 512-520.

562 Fox, J. D., Capadona, J. R., Marasco, P. D., & Rowan, S. J. (2013). Bioinspired
563 water-enhanced mechanical gradient nanocomposite films that mimic the architecture
564 and properties of the squid beak. Journal of the American Chemical Society, 135,
565 5167-5174.

566 Fu, L., Wu, F., Xu, C., Cao, T., Wang, R., & Guo, S. (2018). Anisotropic shape
567 memory behaviors of polylactic acid/citric acid–bentonite composite with a gradient
568 filler concentration in thickness direction. Industrial & Engineering Chemistry

569 Research, 57, 6265-6274.

570 Gan, L., Dong, M., Han, Y., Xiao, Y., Yang, L., & Huang, J. (2018). Connection-
571 improved conductive network of carbon nanotubes in a rubber cross-link network.
572 ACS Applied Materials & Interfaces, 10, 18213-18219.

573 Goetz, L., Mathew, A., Oksman, K., Gatenholm, P., & Ragauskas, A. J. (2009). A
574 novel nanocomposite film prepared from crosslinked cellulosic whiskers
575 Carbohydrate Polymers, 75, 85-89.

576 Goetz, L., Foston, M., Mathew, A. P., Oksman, K., & Ragauskas, A. J. (2010).
577 Poly(methyl vinyl ether-*co*-maleic acid)-polyethylene glycol nanocomposites cross-
578 linked in situ with cellulose nanowhiskers. Biomacromolecules, 11, 2660-2666.

579 Jardin, J. M., Zhang, Z., Hu, G., Tam, K. C., & Mekonnen, T. H. (2020).
580 Reinforcement of rubber nanocomposite thin sheets by percolation of pristine
581 cellulose nanocrystals. International Journal of Biological Macromolecules, 152, 428-
582 436.

583 Jiang, M., Zhang, J., Wang, Y., Ahmad, I., Guo, X., Cao, L., Chen, Y., Gan, L.&
584 Huang, J. (2021). Covalent-bond-forming method to reinforce rubber with cellulose
585 nanocrystal based on the thiol-ene click reaction. Composites Communications, 27,
586 100865.

587 Joseph, E., & Singhvi, G. (2019). Multifunctional nanocrystals for cancer therapy: a
588 potential nanocarrier. In A. M. Grumezescu (Ed.), *Nanomaterials for drug delivery*
589 *and therapy* (pp. 91-116). Elsevier Inc.

590 Kawahara, S., Chaikumpollert, O., Sakurai, S., Yamamoto, Y., & Akabori, K. (2009).
591 Crosslinking junctions of vulcanized natural rubber analyzed by solid-state NMR
592 spectroscopy equipped with field-gradient-magic angle spinning probe. Polymer, 50,
593 1626-1631.

594 Liu, Y., Cao, L., Yuan, D., & Chen, Y. (2018). Design of super-tough co-continuous

595 PLA/NR/SiO_2 TPVs with balanced stiffness-toughness based on reinforced rubber
596 and interfacial compatibilization. Composites Science & Technology, 165, 231-239.

597 Neto, W. P. F., Mariano, M., da Silva, I. S. V., Silvério, H. A., Putaux, J.-L., Otaguro,
598 H., Pasquini, D., & Dufresne, A. (2016). Mechanical properties of natural rubber
599 nanocomposites reinforced with high aspect ratio cellulose nanocrystals isolated from
600 soy hulls. Carbohydrate Polymers, 153, 143-152.

601 Ning, Y., Xie, H., Xing, H., Deng, W., & Yang, D. (1996). Comparison of self-
602 assembled monolayers of *n*-alkanethiols and phenylthioureas on the surface of gold.
603 Surface and Interface Analysis, 24, 667-670.

604 Parambath Kanoth, B., Claudino, M., Johansson, M., Berglund, L. A., & Zhou, Q.
605 (2015). Biocomposites from natural rubber: Synergistic effects of functionalized
606 cellulose nanocrystals as both reinforcing and cross-linking agents via free-radical
607 thiol–ene chemistry. ACS Applied Materials & Interfaces, 7, 16303-16310.

608 Pasquini, D., de Morais Teixeira, E., da Silva Curvelo, A. A., Belgacem, M. N., &
609 Dufresne, A. (2010). Extraction of cellulose whiskers from cassava bagasse and their
610 applications as reinforcing agent in natural rubber. Industrial Crops & Products, 32,
611 486-490.

612 Peng, C., Yang, Q., Zhao, W., Ren, J., Yu, Q., Hu, Y., & Zhang, X. (2019).
613 Relationship between interface chemistry and reinforcement in
614 polybutadiene/cellulose nanocrystal nanocomposites. Composites Science &
615 Technology, 177, 103-110.

616 Shanmuganathan, K., Capadona, J. R., Rowan, S. J., & Weder, C. (2010). Bio-
617 inspired mechanically-adaptive nanocomposites derived from cotton cellulose
618 whiskers. Journal of Materials Chemistry, 20, 180-186.

619 Smyth, M., García, A., Rader, C., Foster, E. J., & Bras, J. (2017). Extraction and
620 process analysis of high aspect ratio cellulose nanocrystals from corn (Zea mays)

621 agricultural residue. Industrial Crops & Products, 108, 257-266.

622 Tang, L., & Weder, C. (2010). Cellulose whisker/epoxy resin nanocomposites. ACS
623 Applied Materials & Interfaces, 2, 1073-1080.

624 Tao, H., Dufresne, A., & Lin, N. (2019). Double-network formation and mechanical
625 enhancement of reducing end-modified cellulose nanocrystals to the thermoplastic
626 elastomer based on click reaction and bulk cross-linking. Macromolecules, 52, 5894-
627 5906.

628 Ulman, A. (1996). Formation and structure of self-assembled monolayers. Chemical
629 Reviews, 96, 1533-1554.

630 Wu, X., Lu, C., Zhang, X., & Zhou, Z. (2015). Conductive natural rubber/carbon
631 black nanocomposites *via* cellulose nanowhisker templated assembly: tailored
632 hierarchical structure leading to synergistic property enhancements. Journal of
633 Materials Chemistry 3, 13317-13323.

634 Xu, C., Zheng, Z., Wu, W., Wang, Z., & Fu, L. (2019). Dynamically vulcanized
635 PP/EPDM blends with balanced stiffness and toughness via in-situ compatibilization
636 of MAA and excess ZnO nanoparticles: Preparation, structure and properties.
637 Composites Part B: Engineering, 160, 147-157.

638 Zhu, G., Xu, H., Dufresne, A., & Lin, N. (2018). High-adsorption, self-extinguishing,
639 thermal, and acoustic-resistance aerogels based on organic and inorganic waste
640 valorization from cellulose nanocrystals and red mud. ACS Sustainable Chemistry &
641 Engineering, 6, 7168-7180.

642 Zhu, G., Chen, Z., Wu, B., & Lin, N. (2019). Dual-enhancement effect of electrostatic
643 adsorption and chemical crosslinking for nanocellulose-based aerogels. Industrial
644 Crops & Products, 139, 111580.

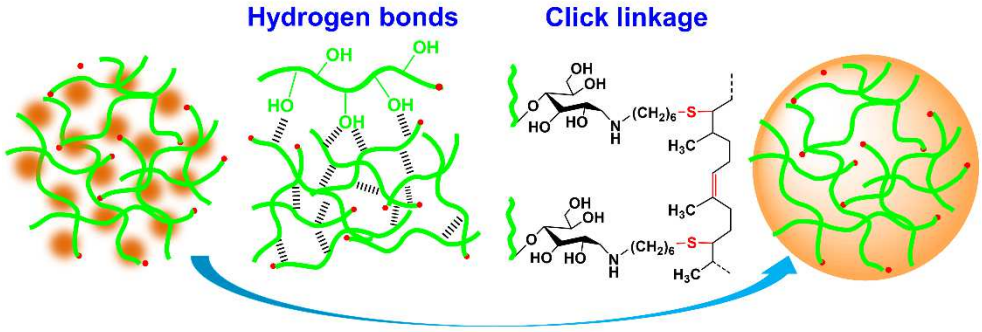
Hydrogen bonds
Click linkage
OH
HO
OH
OH
OH
OH
HO
HO
O
N
H
(CH2)6
S
H3C
H3C